Ballistic quantum transport at high energies and high magnetic fields

S. Rotter, B. Weingartner, N. Rohringer, and J. Burgdörfer

Institute for Theoretical Physics, Vienna University of Technology, Wiedner-Hauptstrasse 8-10, A-1040 Vienna, Austria

We present an extension of the modular recursive Green's function method for ballistic quantum transport to include magnetic fields. Dividing the nonseparable two-dimensional scattering problem into separable substructures allows us to calculate transport coefficients and scattering wave functions very efficiently. Previously unattainable energy and magnetic-field regions can thereby be covered with high accuracy. The method is applied to magnetotransport through a circle and a stadium shaped quantum dot at strong magnetic fields and high energies. In the few edge state regime we observe strong multifrequency Aharonov-Bohm oscillations. By analyzing them in terms of a multichannel interference model, we classify these fluctuations within the framework of Fano resonances and discuss their geometry independence. For high energies (mode numbers) we observe localization of the scattering wave function near classical trajectories.

I. INTRODUCTION

Accurate simulations of ballistic transport through quantum dots have remained a computational challenge, despite the conceptional simplicity of the problem. This is in part due to the fact that many of the most interesting phenomena occur in a parameter regime of either high magnetic field B or high Fermi energy E_F. The regime of strong magnetic field B, where the magnetic length (in a.u.) $l_B = \sqrt{c/B}$ is small compared to the linear dimension D of the dot, $l_B \ll D$, gives rise to the quantum Hall effect,[1,2] the Hofstadter butterfly,[3] and Aharonov-Bohm oscillations of transport coefficients.[4] The high-energy domain, where the de Broglie wavelength $\lambda_D = \sqrt{2E_F}$ satisfies $\lambda_D \ll D$, is of particular relevance for approaching the semiclassical limit of quantum transport and for investigations of quantum signatures of classical chaos.[5–7] Both these regimes pose considerable difficulties for a numerical treatment. Methods based on the expansion of the scattering wave function in plane or spherical waves become invalid at high fields since diamagnetic contributions are generally neglected.[8] Methods employing a discretization on a grid are limited by the constraint that the magnetic flux per unit cell must be small, which, in turn, requires high grid densities for large B.[9] The same requirement has to be met for high E_F, where many grid points are needed to accurately describe the continuum limit. This implies, however, a large number of inversions of high-dimensional matrices, and therefore limits the applicability of these approaches for large B and (or) large E_F.

In the present paper we propose an approach that allows accurate treatment of these regimes. We present an extension of the previously[10] introduced *modular recursive Green's function method* (MRGM) to include an additional magnetic field perpendicular to the two-dimensional scattering surface. The underlying idea for our approach goes back to the work of Sols *et al.*[11] and to the widely used *recursive Green's function method* (RGM).[9,12] In the standard RGM the Green's function is propagated through the scattering region from one transverse strip to the next by repeated solutions of a matrix Dyson equation. We show that the efficiency of this conventional discretization can be increased considerably by

taking the symmetries of a scattering problem into account from the outset. Specifically, when the two-dimensional nonseparable open quantum dot can be built up out of simpler separable substructures (referred to in the following as modules), the Green's function for each of these modules can be calculated efficiently and virtually exactly. Calculation of the S matrix and of the scattering wave function is thus reduced to ''welding'' together the modules by a very small number of recursions. Key to this approach are tight-binding grids which are symmetry adapted for each module. This leads to the separability of the eigenfunctions in the modules and allows an efficient incorporation of boundary conditions. As a result, a much higher grid density can be easily handled, which, in turn, is a prerequisite for treating short magnetic lengths l_B and short wave lengths λ_D. Matrix Dyson equations have to be solved only for each junction between the modules. The total number of necessary recursions (i.e., high-dimensional matrix inversions) is thereby reduced to the number of modules needed to reconstruct the quantum dot.

The efficiency of the MRGM will be demonstrated by applying it to transport through a circular and a stadium shaped quantum dot. These systems are known as prototype structures for regular and chaotic dynamics, and have been studied thoroughly in the literature.[5–7,13] Concerning the theoretical approaches for the investigation of electron dynamics in quantum dots, considerable attention has been dedicated to reach higher energies[14–18] and higher magnetic fields.[17,19–23] Especially for the study of transport through open stadium billiards, several different methods have been employed.[8,16,24–27] In the following we will present numerical results obtained by the MRGM, which attain a parameter range, which, to our knowledge, is not yet explored by other approaches. For small λ_D we investigate the localization of the scattering wave function near classical scattering trajectories. Characteristic differences in the dynamics of generically regular and chaotic systems will be highlighted. In the high-magnetic-field regime, which is governed by edge states, differences between the dynamics in different geometries disappear and are replaced by universal quasiperiodic conductance oscillations. At a critical magnetic field, these

oscillations break off and transport terminates entirely. In the regime where more than one edge state is excited in the dot, we find interference fluctuations, which we analyze in terms of a multichannel Fano interference model.[28] The key to the understanding of the observed fluctuations is that interchannel scattering between different edge states takes place only by diffractive scattering at the lead junctions.

This paper is organized as follows. In Sec. II the method for inclusion of a magnetic field in the MRGM is presented. Section III is dedicated to a discussion of numerical results, illustrating the high-magnetic-field and high-energy behavior in quantum dots. The paper concludes with a short summary in Sec. IV.

II. METHOD

We consider ballistic nanostructures with a constant electrostatic potential inside the two-dimensional cavity, impose hard-wall boundary conditions, and assume a constant magnetic field B to be oriented perpendicular to the scattering plane. The shape of the quantum dot will be chosen to be either a circle or a stadium (see Figs. 5 and 6 below), which represent prototype systems for regular and chaotic classical dynamics, respectively. Two semi-infinite waveguides of width d at different electrochemical potentials μ_1 and μ_2 are attached. The aperture of the leads is chosen to be very small, $d/D = d/\sqrt{A^{\text{dot}}} = 0.0935$, where $A^{\text{dot}} = 4 + \pi$ is the scaled area of all the cavities studied and D is a characteristic linear dimension of the cavity. At asymptotic distances, i.e., far away from the quantum dot, scattering boundary conditions are imposed. The asymptotic scattering state can be factorized into a longitudinal flux-carrying plane wave and a transverse standing wave. The latter is a simple sine wave in the field-free case and a combination of Kummer functions when the magnetic field is turned on.[29,30] In our local coordinate system the longitudinal (transverse) direction in the ith lead is always denoted by x_i (y_i). The wave functions in the waveguides thus vanish at $y_i = \pm d/2$. Atomic units ($\hbar = |e| = m_{\text{eff}} = 1$) will be used from now on, unless explicitly stated otherwise.

A. Brief review of the MRGM

In order to highlight the technical difficulties in incorporating a magnetic field we start by briefly reviewing the MRGM for the field-free case. Our starting point is the observation that a large class of dot geometries with nonseparable boundaries can be decomposed into separable two-dimensional substructures, referred to in the following as modules. For each of these modules the discretization of the corresponding tight-binding (tb) Hamiltonian can be performed on a symmetry-adapted grid. The grid for each module is chosen such that the eigenfunctions of the tb Hamiltonian,

$$\hat{H}^{\text{tb}} = \sum_i \varepsilon_i |i\rangle\langle i| + \sum_{i,j} V_{i,j} |i\rangle\langle j|, \qquad (2.1)$$

separate into two generalized coordinates. $\hat{H}^{\text{tb}}$ contains hopping potentials $V_{i,j}$ for nearest-neighbor coupling and site energies ε_i. Both quantities are chosen such that the Schrödinger equation $\hat{H}^{\text{tb}}|\psi_m\rangle = E_m|\psi_m\rangle$ converges towards the continuum Schrödinger equation in the limit of high grid point density. The most straightforward application of this approach refers to modules for which the boundaries are nodal lines of Cartesian (x,y) or polar coordinates (ϱ,φ). For these coordinate systems, we have[10] at $B=0$

$$V_{i,i\pm1}^x = \frac{-1}{2\Delta x^2}, \quad V_{j,j\pm1}^y = \frac{-1}{2\Delta y^2}, \quad \varepsilon_i = \frac{1}{\Delta x^2} + \frac{1}{\Delta y^2},$$
$$(2.2a)$$

$$V_{i,i\pm1}^\varrho = \frac{-\varrho_{i\pm1/2}}{2\varrho_i\Delta\varrho^2}, \quad V_{j,j\pm1}^\varphi = \frac{-1}{2\varrho_i^2\Delta\varphi^2},$$

$$\varepsilon_i = \frac{1}{\Delta\varrho^2} + \frac{1}{\varrho_i^2\Delta\varphi^2}, \qquad (2.2b)$$

with $\varrho_i = |i - 1/2|\Delta\varrho$. For separable energy eigenfunctions of the general form $|E_m\rangle = |E_k\rangle \otimes |E_{k,n}\rangle$, the spectral representation of the retarded $(+)$ and advanced $(-)$ Green's function $G^\pm(\mathbf{r},\mathbf{r}',B,E_F)$ of the module is simply given by

$$G^\pm(\mathbf{r},\mathbf{r}',B,E_F) = \sum_k \langle\alpha|E_k\rangle\langle E_k|\alpha'\rangle \sum_n \frac{\langle\beta|E_{kn}\rangle\langle E_{kn}|\beta'\rangle}{E_F \pm i\varepsilon - E_{kn}}, \qquad (2.3)$$

where (α,β) stand for the (generalized) coordinates (x,y) or (ρ,φ). The indices (k,n) represent the quantum numbers of the separable eigenfunctions $|E_k\rangle, |E_{k,m}\rangle$ associated with the degrees of freedom α and β, respectively.

The Green's functions of the separate modules are joined by solving a matrix Dyson equation,

$$G = G^0 + G^0 \bar{V} G, \qquad (2.4)$$

where G^0 and G denote Green's functions of the disconnected and the connected modules, respectively. The matrix $\bar{V}$ denotes the hopping potential V multiplied by the size of the unit cell, $\bar{V} = V\Delta_R$, which in a Cartesian (polar) grid is $\Delta_R = \Delta x\Delta y (= \varrho_i\Delta\varrho\Delta\varphi)$. The complete scattering structure can thus be assembled from the individual modules (much like a jigsaw puzzle). The number of necessary recursions [i.e., solutions of Eq. (2.4)] is (approximately) equal to the number of modules. The exact number depends on the number of link modules required for different grid structures. For example, in order to connect a half circle with a rectangle, we need one additional link module which is plugged in between [see Ref. 10 for details]. The key property of these link modules is their adaption to two different grid symmetries [see Fig. 3(b)]. Mathematically speaking, the transition from a polar to a Cartesian grid requires a link module in order to preserve the Hermiticity of the tb Hamiltonian at the junction. In the recursion, the link module is connected to the Cartesian (polar) grid by means of the hopping potential $\bar{V}^x(\bar{V}^\varphi)$. In addition we avoid spurious reflections that would arise at the junction between modules of a different grid structure.

Once the Green's function G^+ for the combination of all modules is assembled, the transmission amplitudes t_{nm} from

entrance lead mode m into exit lead mode n can be calculated by projecting G^+ onto the transverse wave functions in the leads $\chi_n(y_i)$. With the corresponding longitudinal wave numbers $k_{x_i,n}$, we have (at $B=0$)

$$t_{nm}(E_F) = -i\sqrt{k_{x_2,n}k_{x_1,m}}\int_{-d/2}^{d/2}dy_2$$
$$\times\int_{-d/2}^{d/2}dy_1\chi_n^*(y_2)\,G^+(y_2,y_1,E_F)\chi_m(y_1).$$
$$(2.5)$$

Together with the reflection amplitudes r_{nm} (for which an analogous relation holds), the S matrix is completely determined and satisfies the unitarity condition implied by current conservation,

$$\sum_{n=1}^{M}(|t_{nm}|^2 + |r_{nm}|^2) = 1. \qquad (2.6)$$

The integer M denotes the number of open channels in the leads. According to the Landauer formula, the total conductance g through the quantum dot is given by

$$g = \frac{1}{\pi}\sum_{m,n=1}^{M}|t_{nm}|^2 = \frac{1}{\pi}T^{\text{tot}}, \quad \text{with} \quad T^{\text{tot}} + R^{\text{tot}} = M. \qquad (2.7)$$

B. Inclusion of the magnetic field

Incorporation of the magnetic field into the MRGM poses a number of complications. The solutions of these difficulties will be presented in this section. At the core of the problem is the preservation of separability of the Schrödinger equation. The usage of gauge transformations as well as of Dyson equations for decomposing nonseparable structures into separable substructures plays a key role in accomplishing this goal. The field $\mathbf{B}=(0,0,B)$ enters the tb Hamiltonian (2.1) by means of a Peierls phase factor,[12,31]

$$V_{\mathbf{r},\mathbf{r}'} \to V_{\mathbf{r},\mathbf{r}'}\cdot\exp\left[(i/c)\int_{\mathbf{r}}^{\mathbf{r}'}\mathbf{A}(\mathbf{x})dx\right], \qquad (2.8)$$

with which the field-free hopping potential $V_{\mathbf{r},\mathbf{r}'}$ is multiplied. The vector potential $\mathbf{A}(\mathbf{r})$ satisfies $\boldsymbol{\nabla}\times\mathbf{A}(\mathbf{r})=\mathbf{B}$. The Peierls phase will, of course, in most cases destroy the separability of the eigenfunctions of $\hat{H}^{\text{tb}}$. These difficulties can be, in part, circumvented by exploiting the gauge freedom of the vector potential, i.e.,

$$\mathbf{A} \to \mathbf{A}' = \mathbf{A} + \boldsymbol{\nabla}\lambda, \qquad (2.9)$$

where $\lambda(\mathbf{r})$ is a scalar function. By an appropriate choice of λ, the wave function remains separable on a given symmetry-adapted grid. Specifically, to preserve separability, we employ the Landau gauge for a Cartesian grid,

$$\mathbf{A} = (-By,0,0), \qquad (2.10a)$$

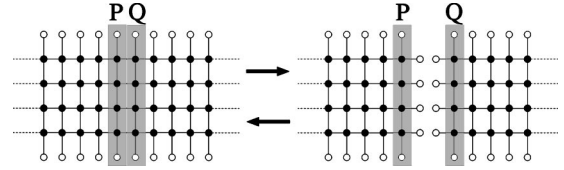and the "symmetric" or circular gauge for a polar grid,

FIG. 1. Joining and disconnecting of modules by application of a Dyson equation: two semi-infinite leads. The hard-wall boundary conditions at the sites on the border of the modules are represented by empty circles (accessible space by full circles). The gray shaded areas P and Q are those grid slices at which the Green's functions are evaluated (see text).

$$\mathbf{A} = B/2(-y,x,0) = \boldsymbol{\rho}\times\mathbf{B}/2. \qquad (2.10b)$$

The scalar gauge potential generating the gauge transformation from Eq. (2.10a) to Eq. (2.10b) is $\lambda(x,y)=Bxy/2$.

A major complication results from the fact that in the presence of the magnetic field the separability on an unrestricted grid of a given symmetry does not imply the separability in the presence of boundary conditions of the *same* symmetry. We illustrate this problem with the help of one typical example, the *semi-infinite* quantum wire with lead width d (Fig. 1). We impose hard-wall boundary conditions $\psi(x,y=\pm d/2)=0$ and consider first the *infinite* quantum wire along the x direction. Because of the Cartesian boundary conditions, the symmetry adapted gauge is the Landau gauge $\mathbf{A}=-By\hat{\mathbf{x}}$. Consider, for notational simplicity, the Schrödinger equation in the continuum limit,

$$H\phi(y,x) = \frac{1}{2}\left(\mathbf{p}+\frac{1}{c}\mathbf{A}\right)^2\phi(x,y)$$
$$= \frac{1}{2}\left(-\frac{\partial^2}{\partial x^2}-\frac{\partial^2}{\partial y^2}-\frac{i2B}{c}y\frac{\partial}{\partial x}+\frac{B^2y^2}{c^2}\right)\phi(x,y)$$
$$= E_F\phi(x,y). \qquad (2.11)$$

Since the longitudinal momentum $p_x = -i\partial/\partial x$ commutes with H, the separability of the wave function persists in the presence of the magnetic field: $\phi(x,y)=f_k(x)\chi(y)$, with $f_k(x)=e^{ikx}$. If, however, one introduces an additional Cartesian boundary condition along the y axis [i.e., $\psi(x=0,y)=0$ for a semi-infinite lead], the situation changes. In the absence of the magnetic field, $B=0$, the linear term in p_x vanishes, and thus the choice $f(x)=\sin(kx)$ [i.e., a linear combination of $f_{\pm k}(x)$] satisfies the boundary condition and preserves the separability, even though p_x is no longer conserved in the semi-infinite lead. However, for $B\neq 0$ and the same boundary condition $\psi(x=0,y)=0$, the term linear in B and p_x destroys the separability. The wave function now takes the general form

$$\phi(x,y) = \sum_m e^{ik_m x}\sum_n c_{mn}\chi_{mn}(y). \qquad (2.12)$$

The breakdown of separability by the introduction of an additional boundary condition indicates that the Green's function of confined modules will be more complex than for extended systems of the same symmetry-adapted grid and

the same gauge. Therefore, the program of the modular method of building up extended complex structures by welding together smaller modules of higher symmetry will be executed in reverse: nonseparable confined modules will be generated by "cutting in pieces" larger separable modules. Confining boundary conditions will be introduced rather than removed by the matrix Dyson equation. In the example above, the semi-infinite quantum wire is generated by cutting the infinite wire at the line $x=0$, thereby imposing the additional boundary condition. Just as connecting modules, so is disconnecting modules equivalent to the application of a matrix Dyson equation,

$$G^E = G^C + G^C \bar{V} G^E. \tag{2.13}$$

In this context, $G^E(G^C)$ is the Green's function of the extended (confined) module and $\bar{V}$ is the hopping potential that connects the modules. Solving Eq. (2.13) *in reversed mode* (i.e., for G^C rather than for G^E) amounts to dissecting the larger module.

Provided that the Green's functions of all the necessary modules are available, we have to link them with each other to assemble the entire scattering geometry. However, in the presence of a magnetic field, we have to take into account that the different modules will be calculated in different symmetry-adapted gauges. Joining different modules requires, therefore, in general a gauge transformation. For the Green's function on the grid $G(\mathbf{r}_i, \mathbf{r}'_j)$, this transformation is simplified by the fact that the matrix of gauge transformations,

$$[\Lambda(\mathbf{r}_j)]_{jk} = \exp[-i\lambda(\mathbf{r}_j)/c] \delta_{jk}, \tag{2.14}$$

is diagonal in the grid representation. Correspondingly, the transformation of both the hopping potential $\bar{V}$ and the Green's function is local, i.e.,

$$\bar{V}(\mathbf{r}_i, \mathbf{r}'_j) \to \bar{V}'(\mathbf{r}_i, \mathbf{r}'_j) = \Lambda(\mathbf{r}_i) \bar{V}(\mathbf{r}_i, \mathbf{r}'_j) \Lambda^*(\mathbf{r}'_j) \tag{2.15}$$

$$G(\mathbf{r}_i, \mathbf{r}'_j) \to G'(\mathbf{r}_i, \mathbf{r}'_j) = \Lambda(\mathbf{r}_i) G(\mathbf{r}_i, \mathbf{r}'_j) \Lambda^*(\mathbf{r}'_j).$$

It is, thus, not necessary to transform gauges of different modules to one global gauge. Instead, it is sufficient to perform a local gauge transformation at the points of the junctions $\{\mathbf{r}_i\}$, such that the gauges of the two modules to be joined agree at these points.

Finally, in order to extract the S matrix, i.e., the amplitudes t_{nm} and r_{nm}, matrix elements of the current operator must be of gauge-invariant form. This requirement can be fulfilled by employing a double-sided gradient operator, which is defined as[32]

$$f\overset{\leftrightarrow}{\mathbf{D}}g = f(\mathbf{x})\mathbf{D}g(\mathbf{x}) - g(\mathbf{x})\mathbf{D}^*f(\mathbf{x}) = -g\overset{\leftrightarrow}{\mathbf{D}}f$$

$$\text{with} \quad \mathbf{D} = \mathbf{\nabla} - \frac{i}{c}\mathbf{A}(\mathbf{x}). \tag{2.16}$$

With its help the transmission amplitudes can be evaluated as[17,32,33]

$$t_{nm}(E_F, B) = -\frac{i}{4\sqrt{\theta_n \theta_m}} \int_{-d/2}^{d/2} dy_2$$

$$\times \int_{-d/2}^{d/2} dy'_1 \chi_n^*(y_2) e^{-ik_n x_2} (\overset{\leftrightarrow}{\mathbf{D}} \cdot \hat{\mathbf{x}}_2)^*$$

$$\times G^+(\mathbf{x}_2, \mathbf{x}'_1, E_F, B)(\overset{\leftrightarrow}{\mathbf{D}}' \cdot \hat{\mathbf{x}}'_1)\chi_m(y'_1) e^{ik_m x'_1}. \tag{2.17}$$

The unit vectors $\hat{\mathbf{x}}_n$ are assumed to be pointing in outward direction of the nth lead and θ_m denotes the outgoing particle flux carried by $\chi_m(y'_1) e^{ik_m x'_1}$ through the lead cross section. Determination of transverse states $\chi_m(y_i)$ and of the corresponding longitudinal momentum k_m as well as the normalization factors θ_m will be discussed below. For reflection amplitudes r_{nm}, a relation similar to Eq. (2.17) holds.[32] From t_{nm} and r_{nm}, the conductance can be calculated by means of the Landauer formula [Eq. (2.7)].

C. Calculation of modules

This section is dedicated to the evaluation of the Green's functions for those modules, which we need to assemble a circle and a stadium billiard: the half-infinite lead, the rectangle, the circle, the half circle, and the link module. With the exception of the circle and the link module, for all these modules Eq. (2.3) is not applicable. This is due to the nonseparability for confined geometries as discussed above. Moreover, the spectrum in open structures like the semi-infinite lead is continuous rather than discrete. Unlike in the field-free case,[34] the resulting integrals cannot be calculated analytically. However, both problems can be overcome by applying a matrix Dyson equation.

1. Rectangular module

As illustrated above for the semi-infinite waveguide, the Dirichlet boundary condition for the confined structure of a rectangle with magnetic field is not separable, no matter which gauge is chosen. The separability can, however, be restored by imposing periodic boundary conditions on two opposing sides of the rectangle. Topologically, this corresponds to folding the rectangle to the surface of a cylinder [Fig. 2(a)]. In this case we connect the first (P) and the last (Q) transverse grid slice of a rectangular grid by a hopping potential $|V_{PQ}^x| = |V_{QP}^x| = -1/2\Delta x^2$. The Green's function of this "cylinder surface" (cs) will be denoted by G^{cs} in the following. The calculation of the rectangle Green's function G^r will be obtained out of G^{cs} by a Dyson equation used here in "reversed" mode, i.e., for *disconnecting* tb grids. This method for calculating the rectangular module may seem like a detour, but it is numerically more efficient than a strip-by-strip recursion. For completeness we mention that an alternative way to calculate G^r was proposed in Ref. 35.

The Green's function for the cylinder surface, G^{cs}, can be constructed from separable eigenfunctions $|E_m\rangle = |E_k^x\rangle \otimes |E_{kn}^y\rangle$, according to Eq. (2.3). Solving the tight-binding Schrödinger equation for the cylinder surface, we obtain for
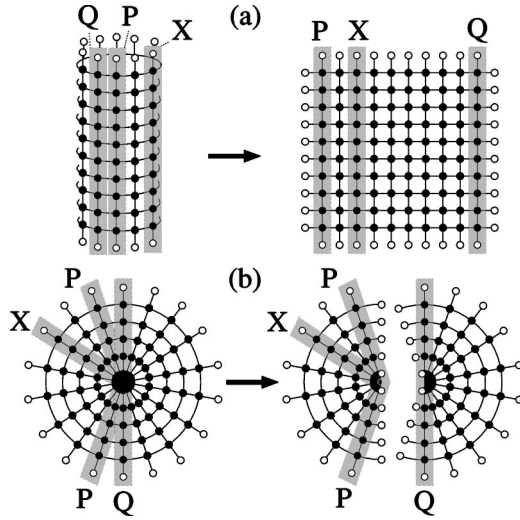
FIG. 2. Applying a Dyson equation in "reversed mode" to construct Green's functions for (a) a rectangle out of a cylinder surface and (b) a semicircle out of a full circle, respectively. In (a) the periodic boundary conditions are transformed into hard-wall boundary conditions. The gray shaded areas P, Q, and X are those grid slices at which the Green's functions are evaluated (see text).

the longitudinal eigenstates $\langle x_j | E_k^x \rangle = (N_x \Delta x)^{-1/2} \exp(i2\pi kj/N_x)$, which results in a tridiagonal, symmetric matrix eigenproblem of size $N_y \times N_y$ for the transverse modes,[36]

$$E_{kn}\langle y_l | E_{kn}^y \rangle = \frac{-1}{\Delta x^2}\left[\cos\left(\frac{2\pi k}{N_x} + \frac{B}{c}y_l\Delta x\right) - 1\right]\langle y_l | E_{kn}^y \rangle$$
$$- \frac{1}{2\Delta y^2}(\langle y_{l-1} | E_{kn}^y \rangle - 2\langle y_l | E_{kn}^y \rangle$$
$$+ \langle y_{l+1} | E_{kn}^y \rangle). \quad (2.18)$$

By "cutting the cylinder surface open" along a line of constant x, we obtain from G^{cs} the desired Green's function G^r for the rectangle [Fig. 2(a)]. We demonstrate this for the rectangle Green's function G_{PX}^r from the first transverse slice P to any other slice X. To determine G_{PX}^r, we solve the following system of Dyson equations:

$$G_{PX}^r = G_{PX}^{cs} - G_{PQ}^r \bar{V}_{QP} G_{PX}^{cs} - G_{PP}^r \bar{V}_{PQ} G_{QX}^{cs} \quad (2.19)$$

$$G_{PQ}^{cs} = G_{PQ}^r + G_{PQ}^r \bar{V}_{QP} G_{PQ}^{cs} + G_{PP}^r \bar{V}_{PQ} G_{QQ}^{cs} \quad (2.20)$$

$$G_{PP}^{cs} = G_{PP}^r + G_{PQ}^r \bar{V}_{QP} G_{PP}^{cs} + G_{PP}^r \bar{V}_{PQ} G_{QP}^{cs}, \quad (2.21)$$

where the first line is the reversed Dyson equation. The three unknowns in the above equations are the Green's functions connecting the slices (P,X), (P,Q), and (P,P), i.e., G_{PX}^r, G_{PQ}^r, G_{PP}^r. By solving these three equations, the unknowns can be uniquely determined.
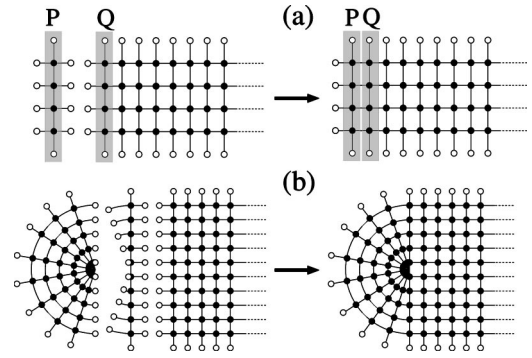

FIG. 3. Applying a Dyson equation to construct Green's functions for (a) a semi-infinite lead and (b) a stadium billiard out of "modules." In (a), joining a transverse slice with a semi-infinite lead schematically leaves the Green's function of the lead invariant. In (b), an additional link module is added to join the half circle and the rectangle module (for details, see Ref. 10). Notation as in Figs. 1 and 2.

2. Circle and half circle

In symmetric gauge, $\mathbf{A} = B/2(-y,x,0)$, the Dirichlet boundary value problem for the circle with magnetic field is separable, $|E_m\rangle = |E_k^\varphi\rangle \otimes |E_{kn}^\varrho\rangle$. On a discrete tb lattice, this statement remains true provided that a circular grid is employed. With the eigenstates for the azimuthal degree of freedom, $\langle \varphi_j | E_k^\varphi \rangle = (N_\varphi \Delta \varphi)^{-1/2}\exp(i2\pi kj/N_\varphi)$ and radial eigenstates $g_{kn}(\varrho_i) = \sqrt{\varrho_i} \times \langle \varrho_i | E_{kn}^\varrho \rangle$, the finite difference equation for the $g_{kn}(\varrho_i)$ results in a tridiagonal symmetric eigenproblem

$$E_{kn} g_{kn}(\varrho_i) = -\frac{1}{\varrho_i^2 \Delta \varphi^2}\left[\cos\left(\frac{2k\pi}{N_\varphi} - \frac{\varrho_i^2 B\Delta\varphi}{2c}\right) - 1\right]g_{kn}(\varrho_i)$$
$$- \frac{1}{2\Delta\varrho^2}\left[\frac{\varrho_{i-1/2}}{\sqrt{\varrho_{i-1}}\sqrt{\varrho_i}}g_{kn}(\varrho_{i-1}) - 2 g_{kn}(\varrho_i)\right.$$
$$\left. + \frac{\varrho_{i+1/2}}{\sqrt{\varrho_i}\sqrt{\varrho_{i+1}}}g_{kn}(\varrho_{i+1})\right]. \quad (2.22)$$

The Green's function for the circular module is then calculated by a straightforward application of Eq. (2.3).

For the Green's function of the half circle, we employ an analogous procedure as in the preceding section: we dissect the circle Green's function into half circles by means of a reversed Dyson equation. We demonstrate this by way of the example depicted in Fig. 2(b), where the "full circle" (fc) is split up into two "half circles" (hc). The resulting two halves are almost identical, with the exception of the two additional radial grid slices, by which the right half circle is larger. For assembling the stadium billiard we have to make sure that the tb grid of the half-circle module can be linked directly to a vertical grid [see Fig. 3(b)]. For this reason, only the left one of the two half circles in Fig. 2(b) can be used for this purpose. Consider as example the Green's function G_{PX}^{hc} describing the propagation from the grid slice P at the junction of the two half-circles to any radial grid slice X situated on

the "left half circle" [see Fig. 2(b)]. G_{PX}^{hc} is determined by the following system of Dyson equations:

$$G_{PX}^{hc} = G_{PX}^{fc} - G_{PP}^{hc} \bar{V}_{PQ} G_{QX}^{fc}, \tag{2.23}$$

$$G_{PP}^{fc} = G_{PP}^{hc} + G_{PP}^{hc} \bar{V}_{PQ} G_{QP}^{fc}, \tag{2.24}$$

which yields a unique solution for G_{PX}^{hc}.

3. Link module

For the field-free case details of the construction of the link module [see Fig. 3(b)] have been discussed in Ref. 10. Due to the "one-dimensional nature" of this module, the additional magnetic-field dependence can simply be incorporated in its Green's function by a multiplication with a gauge phase factor [see Eq. (2.14)].

4. Semi-infinite lead

Because of its continuous spectrum, the Green's function for the semi-infinite lead poses an additional challenge beyond that of the nonseparability of the wave function discussed above. We therefore apply one further "trick" to bypass this problem. Our approach is based on the observation that adding a slice to a semi-infinite quantum wire leaves this wire (up to irrelevant phases) invariant [see Fig. 3(a)]. We assume a semi-infinite lead with $x \in [\Delta x, \infty)$ and hard-wall boundary conditions at $x=0$ and $y=\pm d/2$. To this object, we add a slice consisting of just one transverse chain of tb grid points which we place at $x=0$. The system of Green's functions for the propagation from the transverse chain at $x=0$ (P) back to itself (P) or to the first transverse slice of the semi-infinite lead (Q) at Δx reads

$$G_{PP} = G_{PP}^0 + G_{PP}^0 \bar{V}_{PQ} G_{QP}, \tag{2.25}$$

$$G_{QP} = G_{QQ}^0 \bar{V}_{QP} G_{PP}. \tag{2.26}$$

Each multiplication involves a matrix product with a dimension equal to the number of transverse grid points. The key point now is that the system of Eqs. (2.25,2.26) can be closed through the invariance condition for the semi-infinite lead, i.e., $G_{PP} = G_{QQ}^0$ [see Fig. 3(a)]. In Landau gauge $\mathbf{A} = (-By,0,0)$, the latter relation does not involve additional gauge phases since these are already contained in the hopping matrix element. We additionally note that an equivalent point of departure for the derivation of G_{PP} is the Bloch condition for states in the lead.[17,33]

Setting $Z = G_{PP} \bar{V}_{QP}$ and using the Hermiticity condition $\bar{V}_{QP} = \bar{V}_{PQ}^* \equiv \bar{V}^*$, Eqs. (2.25,2.26) can be converted to a quadratic matrix equation

$$ZZ - \bar{V}^{-1}(G_{PP}^0)^{-1}Z + \bar{V}^{-1}\bar{V}^* = 0. \tag{2.27}$$

Solvents Z of a quadratic matrix equation $Q(Z)=0$ can be constructed from the eigenpairs (β_i, χ_i) of the corresponding quadratic eigenvalue equation $Q(\beta_i)\chi_i = 0$, $i \in [1, \ldots, 2N]$, in the diagonal form,[37]

$$Z = MBM^{-1} \text{ with } M = [\chi_1, \ldots, \chi_N], \ B = \text{diag}(\beta_i). \tag{2.28}$$

The quadratic eigenvalue equation is equivalent to a generalized eigenvalue problem $A\tilde{\chi} = \beta C\tilde{\chi}$ of twice the original dimension.[36] Its $2N$-dimensional eigenvectors $\tilde{\chi} = (\chi, \beta\chi)$ are solutions of the symmetric eigenproblem

$$\begin{pmatrix} -\bar{V}^* & 0 \\ 0 & \bar{V} \end{pmatrix} \begin{pmatrix} \chi \\ \beta\chi \end{pmatrix} = \beta \begin{pmatrix} -(G_{PP}^0)^{-1} & \bar{V} \\ \bar{V} & 0 \end{pmatrix} \begin{pmatrix} \chi \\ \beta\chi \end{pmatrix}, \tag{2.29}$$

where $(G_{PP}^0)^{-1} = E_F - \hat{H}_{1D}^{tb}$ and $\hat{H}_{1D}^{tb}$ is the Hamiltonian of the one-dimensional transverse tb strip at $x=0$. The Fermi energy E_F and the magnetic field B enter Eq. (2.29) as independent parameters at which the eigenstates $\tilde{\chi}_m$ and eigenvalues β_m are evaluated. The longitudinal momenta of the lead states $\xi_m(x,y) = \chi_m(y)e^{ik_m x}/\sqrt{\theta_m}$ are related to the eigenvalues by the relation $\beta = \exp(ik\Delta x)$. The orthonormalization and the completeness relations of the $2N$ eigenvectors $\tilde{\chi}_m$ can be formulated in terms of matrix relations for the generalized eigenproblem,

$$\frac{1}{\sqrt{\theta_m \theta_n}} \tilde{\chi}_m^T C \tilde{\chi}_n = 2i \frac{k_m}{|k_m|} \delta_{mn}$$

$$\text{and} \quad \sum_m^{2N} \frac{\tilde{\chi}_m \tilde{\chi}_m^T}{\theta_m} = 2i \frac{k_m}{|k_m|} C^{-1}. \tag{2.30}$$

With this specific choice of normalization the norm factors θ_m are determined such that every propagating state carries unit flux. We note parenthetically that the quadratic eigenvalue equation could also be applied to the semi-infinite lead at zero B field. However, in that case the Green's function for quantum wires can be calculated analytically[10,34] by complex contour integration.

5. Scattering wave functions and efficiency of the MRGM

The MRGM is particularly well suited to determine transport coefficients as the Green's function is then required only at the junctions between the modules and does not have to be evaluated throughout the interior of the entire quantum dot. Since for the calculation of the scattering wave function the Green's function throughout the entire scattering region is needed, this particular advantage is lost. However, also in this case, the MRGM is still more efficient than the standard RGM, as will be explained below.

The wave function $\psi(\mathbf{x})$ can be obtained at any point $\mathbf{x}$ by projecting the retarded Green's function (by means of the operator $\vec{\mathbf{D}}$) on the incoming wave (in mode m),[17,32]

$$\psi_m(\mathbf{x}) = -\frac{1}{2\sqrt{\theta_m}} \int_{-d/2}^{d/2} dy_1' G^+(\mathbf{x}, \mathbf{x}', E_F, B)$$

$$\times (\vec{\mathbf{D}}' \cdot \hat{\mathbf{x}}_1') \chi_m(y_1') e^{ik_m x_1'}. \tag{2.31}$$

G^+ contains the solution of the Dyson equations for all linked modules. That the evaluation of Eq. (2.31) can be

done very efficiently results from two properties. First, the number of recursions (i.e., of matrix inversions) needed to obtain G^+ is given by the fixed number of modules required to build up the scattering structure. This number is independent of the de Broglie wavelength. The latter enters only in terms of the size of the matrices involved in the recursion, since with increasing E_F (decreasing λ_D) more grid points are required to represent the continuum limit. Compared to the standard RGM the numerical effort is reduced since in that approach the number of recursions scales with the grid density, i.e. $\propto k_F$. A second advantage of the MRGM concerns the incorporation of the boundary conditions. In the modular method the boundaries coincide with the nodal lines of the symmetry-adapted coordinate system for the module. For this reason the convergence towards the continuum limit is enhanced as compared to the slice-by-slice recursion. The calculation of the transport coefficients as a function of the Fermi wave number k_F (or Fermi energy E_F) is simplified by the fact that the solution of the eigenvalue problem $(|E_m\rangle, E_m)$ entering the Green's function for each module [Eq. (2.3)] is independent of E_F. For the evaluation of the Green's function at different values of E_F, the eigenproblem $\hat{H}^{tb}|E_m\rangle = E_m|E_m\rangle$ therefore has to be solved only once. Unfortunately, this feature does not extend to the variation of the magnetic field since both $|E_m\rangle$ and E_m are dependent on B. Because of this property, a new solution of the tb eigenproblem is required for each value of the field. The most severe restriction of the MRGM is, however, that its applicability is limited to those scattering structures which can be assembled from or cut out of separable modules. Also, random potentials and soft walls can only be included as long as they preserve the separability of each module. We mention at this point that a ''hybrid RGM'' for dealing with arbitrary boundary geometries was presented in the literature.[17]

III. NUMERICAL RESULTS FOR HIGH B FIELDS AND LARGE k_F

In this section we present first magnetoconductance results which were calculated with the MRGM at high magnetic fields B and large Fermi wave numbers k_F. As prototype shapes of the cavity we use the circle and the Bunimovich stadium and consider different geometries for the attached quantum wires.

A. Accuracy checks

Several checks for the accuracy of the numerical results have been performed. Exact relationships for transport coefficients such as conservation of unitarity and the Onsager relations are fulfilled with an accuracy greater than 10^{-10}. The grid density is chosen such that the magnetic flux per unit cell is $B\Delta_r/c < 0.01$ (as in Ref. 38). The typical number of grid points per Fermi half wavelength is greater than 30. Only for very high energy calculations (Fig. 5) the relative grid density is lower. For low magnetic fields, we can compare our results for $|t_{nm}(k_F)|^2$ with previous methods. As an example we show in Fig. 4 a comparison for $|t_{11}(k_F)|^2$ with the calculation by Yang et al.,[8] which is based on a wave-
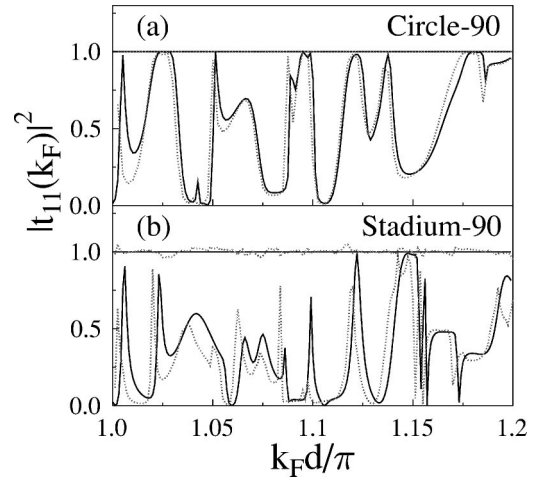

FIG. 4. Comparison between the present MRGM (solid line) and the wave-function matching technique (Ref. 8) (dotted line) for the first-mode transmission probability $|t_{11}(k_F)|^2$ at $B/c = 1$ in a small window of k_F: (a) circle with perpendicular leads and (b) stadium with perpendicular leads ($d = 0.35$, $A^{dot} = 4 + \pi$). In both cases, $|t_{11}(k_F)|^2 + |r_{11}(k_F)|^2$ is also shown. Contrary to the MRGM (solid line), the wave-function matching technique (dotted line) deviates from the unitarity limit in (b).

function expansion in spherical waves. The agreement for the circle is very good, although diamagnetic terms are neglected in the approach of Ref. 8. For the stadium, the differences between the two methods are somewhat larger. This is in part due to the fact that the expansion of the stadium wave functions in spherical waves leads to a unitarity deficiency [see Fig. 4(b)]. We can also reproduce previous results of Ref. 8 concerning weak-localization line shapes and statistical magnetoconductance properties in chaotic and regular cavities. These will not be treated again. Our focus will be on the high magnetic field and high-energy regime where other methods failed.

B. Wave functions

The starting point for the analysis of the scattering states $\psi(\mathbf{x})$ for ballistic transport through quantum dots is Eq. (2.31). Figures 5 and 6 display the resulting electron density $\propto |\psi(\mathbf{r})|^2$ in the scattering region. In Fig. 5 we consider the wave functions at very high k_F for both the circle and the stadium billiard, which are prototypical structures for regular and chaotic dynamics, respectively. Large k_F corresponds to the regime where the convergence towards classical scattering trajectories is expected to emerge. Figures 5(a) and 5(b) illustrate the different dynamics for an injection at high ($m = 20$) and at low mode numbers ($m = 1$), respectively. Since high mode numbers correspond classically to a large injection angle, the wave function condenses around a pentagon-shaped whispering gallery trajectory. For low-mode injection, a small circle representing the centrifugal barrier (or caustic) is seen, as well as rays representing the asterisk orbits.[39] Figures 5(c) and 5(d) display scattering states for the stadium. At low magnetic fields, the dynamics is chaotic and
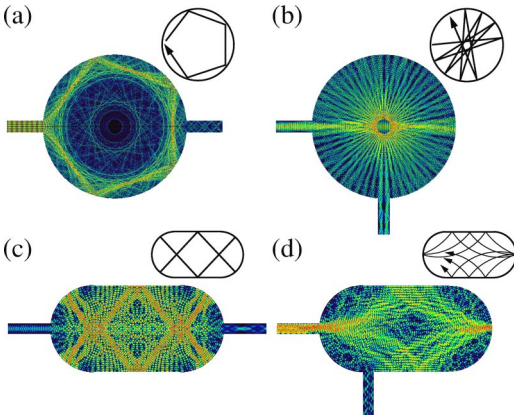
FIG. 5. (Color online) Absolute square of the scattering wave functions $|\psi(x,y)|^2$ at high k_F [(a) $k_F=25\pi/d$, (b) $k_F=12.5\pi/d$, (c,d) $k_F=6.01\pi/d$] for the four quantum dots considered: circle and stadium with relative lead orientation of 90° and 180°, area $A^{dot}=4+\pi$, and lead width $d=0.25$. The localization around classical trajectories (see insets for comparison) is clearly visible. In (a–c) the magnetic field $B=0$. In (d), the magnetic field $B/c=30.5$ allows for a whole bundle of equivalent trajectories with cyclotron radius $r_c=k_Fc/B\approx2.48$ to contribute to transport.

a typical wave function features a quasirandom pattern with a modest density enhancement near classically unstable periodic orbits (not shown). For special values of k_F and B, "scars" emerge in the scattering wave functions [Fig. 5(c)]. By contrast, for high magnetic fields, the classical motion becomes regular. In the present example [Fig. 5(d)]. The wave function condenses around a "bundle" of cyclotron orbits executing three bounces at the cavity wall before exiting through the entrance lead. There has been an extensive discussion in the literature as to the existence of scars in
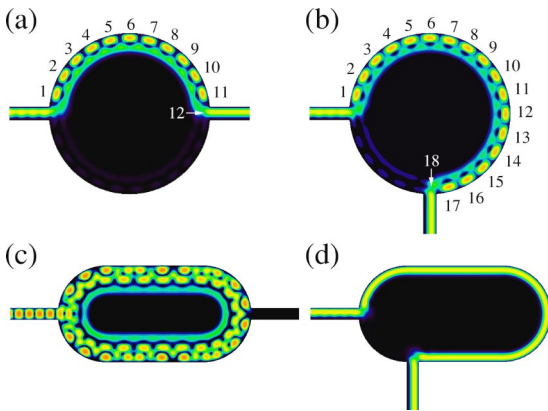

FIG. 6. (Color online) Absolute square of the scattering wave functions $|\psi(x,y)|^2$ in the edge state regime. The area of all geometries, $A^{dot}=4+\pi$, lead width $d=0.25$, and $k_F=1.5\pi/d$. The four plots correspond to the points in the transmission spectra (Fig. 7), indicated by (a–d). The numbers along the longitudinal direction of the edge states count the number of antinodes between entrance and exit leads (see corresponding numbers in Fig. 7). Note that edge states in the magnetic field region $B_c^{n+1}<B<B_c^n$ have up to n transverse nodes: (a) circle, 180°, $n=2$, (b) circle, 90°, $n=2$, (c) stadium, 180°, $n=3$, and (d) stadium, 90°, $n=1$.
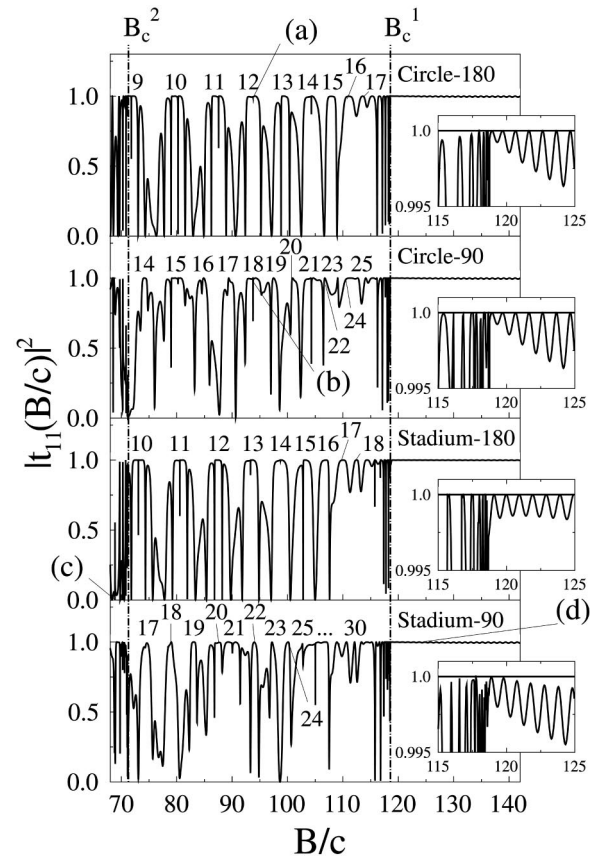

FIG. 7. Transmission probabilities $|t_{11}(B/c)|^2$ in the high-magnetic-field limit for circle and stadium billiard with 180° or 90° lead orientation ($k_F=1.5\pi/d, d=0.25$). B_c^1 and B_c^2 are the threshold magnetic fields $B_c^n/c=k_F^2/(2n+1)$ (vertical dash-dotted lines). Above B_c^1, regular oscillations appear (see insets for magnification). For $B_c^2<B<B_c^1$, irregular fluctuations set in. Their large-scale structure can be explained by the number of interference maxima the two edge states form along the boundary between entrance and exit lead (see indicated numbers). Points (a–d) correspond to the wave functions shown in Fig. 6.

open quantum billiards.[16] Our present results clearly underscore that scars, defined here as the condensation of the wave function near classical (not necessarily unstable) trajectories, clearly exist for large k_F. Figure 6 illustrates the formation of edge states at high fields. With increasing B, fewer edge states can be excited in the cavity. In Fig. 6(c) ($B=68.5$), three transverse edge states are present; while in Fig. 6(d) ($B=125$), only a single edge state remains. For two edge states carrying flux across the quantum dot, interferences give rise to a stationary nodal pattern with a fixed number of antinodes along the boundary [see Figs. 6(a) and 6(b)]. We note that we are not aware of any other method that has so far been capable of investigating scattering states of open structures in this high-magnetic-field regime.

C. Transport coefficients

The interference between different edge states gives rise to characteristic fluctuations in the transport coefficients. Figure 7 shows the high-magnetic-field regime of the trans-
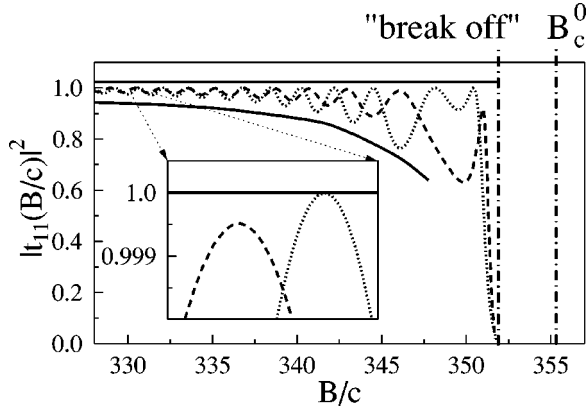
FIG. 8. Transmission probabilities $|t_{11}(B/c)|^2$ in the high-field limit, near the point where transport terminates. The dotted line stands for the circle billiards with both 90° and 180° lead orientation (their transmission probabilities are identical) and the dashed line for the stadium billiard with 90° lead geometry. The solid curves represent the upper and lower bounds of the oscillations (offset for better visibility). The two dash-dotted vertical lines mark the point where transport breaks off and the analytically determined threshold value $B_c^0 \approx 355.3$ (see text for details). The inset shows that the transmission probabilities for the circle reach the maximum value 1, which is only approximately true for the stadium with 90° lead geometry.

mission probability in the first mode $m = n = 1$ for both circle and stadium. Different orientations of the exiting quantum wire were chosen (oriented 90° and 180° relative to the incoming lead). A few universal trends are easily discernible. Above a certain critical value of the magnetic field (denoted by B_c^1), the strongly fluctuating transmission probability gives way to very regular oscillations in all four cases [see insets of Fig. 7 for magnification]. The threshold value B_c^1 and the magnetic field, at which transport is terminated (separately displayed in Fig. 8), are identical for all systems investigated. Below B_c^1, the transport signal displays "beats," i.e., the Fourier transform of the signal is characterized by several frequencies. The "universality" (i.e., geometry independence) of these features is related to the fact that in the high-magnetic-field regime, transport is controlled by edge states (as depicted in Fig. 6). These states play a very prominent role in the quantum Hall effect and have been studied extensively.[1,2,12,40,41] At magnetic fields, where the magnetic length is smaller than the system dimensions, $l_B \ll D$, they are the only states coupling to the quantum wire since bulk Landau states cannot be accessed by the leads. The edge states shown in Figs. 6(a–d) correspond to the points (a)–(d) in the transmission spectrum in Fig. 7. By comparison with the scattering wave functions (as in Fig. 6), we observe that in the magnetic field region, $B_c^n < B < B_c^{n-1}$, edge states have up to $n-1$ transverse nodes in the direction perpendicular to the boundary. Furthermore, the number of longitudinal antinodes from entrance to the exit lead [see the corresponding numbers in Figs. 6(a,b)] can be directly mapped onto successive maxima in Fig. 7 (see numbers there). The range of B depicted in Fig. 7 corresponds to B
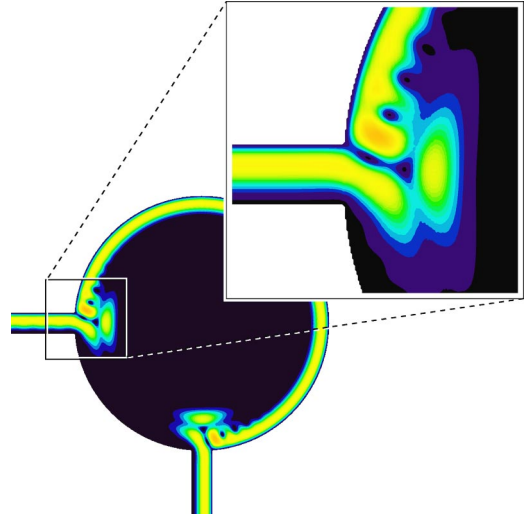

FIG. 9. (Color online) Electron density $|\psi(x,y)|^2$ for the circle billiard with diffractive scattering highlighted. ($A^{\text{dot}} = 4 + \pi$, lead width $d = 0.25$, and $k_F = 1.5\pi/d$.) The magnetic field $B = 118.7$ is just above the threshold to the single-edge state regime $B_c^1 = 118.44$.

$\gtrsim B_c^2$ at $k_F = 1.5\pi/d$. The transmission spectrum becomes increasingly complex as B is reduced, or equivalently, k_F is increased (not shown).

To determine the positions of the values B_c^n, we consider the energy shift of Landau levels near the boundary. Bulk Landau levels are degenerate since their quantized energy $E_n = (n + 1/2)B/c$ is independent of their position in space. This degeneracy is lifted if a Landau state is placed in the vicinity of the cavity wall: with decreasing distance to this boundary, the energy of the state increases. Therefore the energies of edge states associated with the quantum number n lie above the asymptotic bulk value E_n. When the incoming electron is diffracted at the mouth of the entrance lead, only those edge states whose energy is below the Fermi energy can carry the flux. Due to the sharp edges at the junction between lead and quantum dot, all energetically accessible edge channels are populated. The blow up of the scattering wave function near the lead mouth (Fig. 9) highlights the diffractive edge scattering. This is in contrast to smooth edges where states in the lead could cross the lead junction adiabatically, i.e., without changing their state of quantization.[42] With sharp lead junctions, however, all edge states with quantum number $n' \leqslant n$ will participate in transport up to a magnetic field where E_n touches the Fermi energy, $E_n = E_F$, i.e., at the critical magnetic fields $B_c^n/c = E_F/(n + 1/2)$. These threshold values are indicated by the dot-dashed vertical bars in Figs. 7 and 8 for $B_c^2 \approx 71.1$, $B_c^1 \approx 118.4$, and $B_c^0 \approx 355.3$ for a lead width $d = 0.25$ and $k_F = 1.5\pi/d$. In our numerical data, both the position of these threshold values as well as their independence of the geometry are in excellent agreement with this prediction. The only exception is the critical magnetic field B_c^0. Its value (355.3) lies slightly above the point where the transmission spectrum ceases (at $B \approx 351.8$) (see Fig. 8). The reason for this deviation is the fact that the termination point of the spectrum is

not determined by the magnetic field of the lowest bulk Landau level in the cavity (i.e., B_c^0), but by the highest field at which the leads still carry flux. In the leads, however, the magnetic length does not satisfy the condition $l_B \ll d$ (at $k_F = 1.5\pi/d$: $l_B \approx d/4.7$). Contrary to the cavity, the lead wave functions still "feel" the constriction by the opposing wall. For this reason the threshold magnetic-field values of the transverse lead states lie slightly below those of the bulk Landau levels, leading to a termination already below B_c^0.

D. Multichannel interferences

The regular oscillations above B_c^1 as well as the complex fluctuating pattern below B_c^1 can be explained by a multi-channel scattering description. This model can be viewed as a generalization[28,45] of a single-channel picture.[2,43,44] For this description to be applicable, the cavity of the dot has to have smooth boundaries and disorder must be absent. Under these circumstances the flux transported by edge states is conserved in the interior and changed only by diffractive scattering at lead junctions. At the junction, a fraction of the flux will exit through the lead while the remaining portion of the flux will continue to propagate along the boundary. The stationary scattering state can be viewed as the coherent superposition of repeated loops around the billiard. In order to translate this picture into an analytic expression, we define amplitudes for transmission and reflection at the two lead junctions. We denote the amplitudes for transmission from transverse mode m in the entrance lead to the edge state in the dot with quantum number i by $\tilde{t}_{mi}$. The amplitudes $\tilde{t}'_{in}$ stand for transmission from edge state i in the dot to the transverse mode n in the exit lead. The amplitudes $\tilde{r}_{ij}(\tilde{r}'_{ij})$ describe edge state reflection at the entrance (exit) lead from mode i to mode j. (The tilde signs serve to distinguish these amplitudes from the transport coefficients for the whole geometry t_{nm} and r_{nm}.) We further define the following matrices:

$$[\tilde{T}]_{ij} = \tilde{t}_{ij} e^{ik_j L_j - iBA_j/c}, \quad [\tilde{T}']_{ij} = \tilde{t}'_{ij}, \quad (3.1)$$

$$[\tilde{R}']_{ij} = \tilde{r}'_{ij} e^{ik_j L'_j - iBA'_j/c}, \quad [\tilde{R}]_{ij} = \tilde{r}_{ij} e^{ik_j L_j - iBA_j/c}, \quad (3.2)$$

where $L_j, A_j (L'_j, A'_j)$ denote the lengths L and areas A the edge state j covers from entrance to exit (from exit to entrance) of the dot. The areas A can be determined in gauge-invariant form, although the corresponding classical orbits are not necessarily periodic.[46] The transmission through the whole cavity $t_{ji} = [T]_{ij}$ is then written as a geometric series of matrices,

$$T = \tilde{T}\{1 + \tilde{R}'\tilde{R}[1 + \tilde{R}'\tilde{R}(1 + \cdots)]\}\tilde{T}'$$

$$= \tilde{T}\left(\sum_{i=0}^{\infty} (\tilde{R}'\tilde{R})^i\right)\tilde{T}'$$

$$= \tilde{T}(1 - \tilde{R}'\tilde{R})^{-1}\tilde{T}'. \quad (3.3)$$

Equation (3.3) serves as a convenient starting point for the analysis of the transmission fluctuations. Consider first the regime $B > B_c^1$, where only the lowest transverse edge state is excited. In this case Eq. (3.3) reduces to its scalar version[2,43,44]

$$T^{\text{tot}} = |t_{11}|^2 = \frac{|\tilde{t}_{11}|^2 |\tilde{t}'_{11}|^2}{1 - 2\text{Re}[\tilde{r}'_{11}\tilde{r}_{11} e^{i\gamma}] + |\tilde{r}'_{11}|^2 |\tilde{r}_{11}|^2}, \quad (3.4)$$

with $\gamma = k_1(L_1 + L'_1) - B(A_1 + A'_1)/c$. As expected, the fluctuations of $|t_{11}(B/c)|^2$ are determined by an Aharonov-Bohm–type phase γ. At fixed k_F, the oscillation period is $\Delta B = 2\pi c/A_1^{\text{tot}}$. By $A_1^{\text{tot}} = A_1 + A'_1$, we denote the area which the edge state acquires in one revolution around the dot. Taking into account that the dynamically accessible area of the edge state is somewhat smaller than the geometric area, $A_1^{\text{tot}} < A^{\text{dot}} = 4 + \pi$ (see Fig. 6), the prediction for the oscillation period is in excellent agreement with our numerical findings. Equation (3.4) also explains why the oscillation period is increasing with increasing B (see Fig. 8). This explanation makes use of the somewhat counterintuitive fact that for increasing magnetic field skipping orbits with fixed quantum number n have an increasing mean distance from the boundary.[44] Consequently, a larger B field implies a smaller enclosed area A_1^{tot} and therefore a higher oscillation period ΔB. Furthermore, Eq. (3.4) accounts for the fact that for most structures the successive maxima of T^{tot} reach unity.[43] (The small deviation from this rule of the stadium with 90° lead orientation will be explained below). In addition to unitarity, $[|\tilde{t}'_{11}|^2 + |\tilde{r}'_{11}|^2 = 1]$, we have for identical lead junctions $\tilde{r}_{11} = \tilde{r}'_{11}$. (We call two junctions *identical* if the local environment of their lead mouths is the same and their respective distance is larger than a few wavelengths.) Above B_c^1, scattering of an edge state at a junction is essentially a one-dimensional process, for which the probability for transmission from left to right has the same magnitude as vice versa. Identical lead junctions therefore also imply $\tilde{t}'_{11} = \tilde{t}_{11}$, provided that the two corners of the lead junction have the same shape. If, and only if, all of the three above conditions are fulfilled, Eq. (3.4) yields $T^{\text{tot}} = 1$ at the resonance condition $\gamma = 2\pi n, n \in \mathbb{Z}$. Since for the two circle geometries and for the 180° stadium the two lead junctions are identical, we indeed find in these cases that $|t_{11}(B)|^2$ periodically reaches unity. On the other hand, when the leads are attached to the stadium at an angle of 90°, one lead is attached to the straight section while the other is attached to the semicircle. The local environment of the two lead mouths is in this case different (i.e., the lead junctions are not identical), for which reason our numerical results do not quite reach $|t_{11}|^2 = 1$, when the resonance condition is fulfilled for this geometry [see the insets of Fig. 7 and Fig. 8]. Another relation exists between the resonance condition and the behavior of edge states. In the closed cavity an edge channel always encloses an integer number of flux quanta $[BA/(\phi_0 c) = m \in \mathbb{N}]$. Therefore, the resonance condition is met whenever the energy of an edge state in the closed cavity crosses the Fermi edge.[44]

One interesting feature of the transmission fluctuations in the single-channel regime of the circular dot ($B > B_c^1$) is their invariance with respect to the lead orientation. The numerical results for the transmission probabilities of the circle with 180° and 90° lead orientation differ only at the tenth decimal digit. This fact, as well as the observation that in the case of the stadium billard the two lead orientations give different results, can again be explained by Eq. (3.4). The important point to note is that the interference phase ($\gamma = k_1 L_1^{\text{tot}} - B A_1^{\text{tot}}/c$) does not change when changing the positions of the leads around the circle. Due to the rotational symmetry, also the coefficients $\tilde{t}_{11}, \tilde{t}'_{11}, \tilde{r}_{11}$, and $\tilde{r}'_{11}$ are the same for different angles between the leads. The same is thus true for the total transmission T^{tot} through the circular dot. The only exception to this rule occurs when the two leads are in close proximity to within a few wavelengths. In this case the transmission probability changes as compared to the results for the 180° and 90° lead orientation (not shown).

The fluctuations in the regime $B < B_c^1$ displayed in Fig. 7 can be analyzed with the help of a multichannel scattering description. In the interval $B_c^2 \lesssim B \lesssim B_c^1$, two channels corresponding to two edge states are open in the cavity and one channel in each of the leads. From the entrance to the exit lead mouth, the two edge channels acquire the phases $e^{ik_1 L_1 - iB A_1/c}$ and $e^{ik_2 L_2 - iB A_2/c}$, respectively. Their interference at the exit lead will therefore give an oscillatory contribution to the total transmission $T^{\text{tot}}(B) = |t_{11}|^2$ of the form $\cos^2[B(A_1 - A_2)/(2c)]$. For closer analysis we need to evaluate Eq. (3.3), which involves the inversion of 2×2 matrices. In the case of parallel lead orientation the corresponding expressions are simplified due to the fact that the phases acquired from entrance to exit lead and vice versa are the same ($A_n = A'_n$ and $L_n = L'_n$),

$$
t_{11} = [e^{i\varphi_1} \tilde{t}_{11} \tilde{t}'_{11} + e^{i\varphi_2} \tilde{t}_{12} \tilde{t}'_{21} + e^{i(2\varphi_1 + \varphi_2)} (\tilde{r}_{11} \tilde{t}_{12} - \tilde{r}_{12} \tilde{t}_{11})
$$

$$
\times (\tilde{r}'_{21} \tilde{t}'_{11} - \tilde{r}'_{11} \tilde{t}'_{21}) + e^{i(\varphi_1 + 2\varphi_2)} (\tilde{r}_{21} \tilde{t}_{12} - \tilde{r}_{22} \tilde{t}_{11})
$$

$$
\times (\tilde{r}'_{22} \tilde{t}'_{11} - \tilde{r}'_{12} \tilde{t}'_{21})] / [1 - e^{i2\varphi_1} \tilde{r}_{11} \tilde{r}'_{11} - e^{i2\varphi_2} \tilde{r}_{22} \tilde{r}'_{22}
$$

$$
- e^{i(\varphi_1 + \varphi_2)} (\tilde{r}_{21} \tilde{r}'_{12} + \tilde{r}_{12} \tilde{r}'_{21}) - e^{i2(\varphi_1 + \varphi_2)} (\tilde{r}_{11} \tilde{r}_{22} - \tilde{r}_{12} \tilde{r}_{21})
$$

$$
\times (\tilde{r}'_{12} \tilde{r}'_{21} - \tilde{r}'_{11} \tilde{r}'_{22})], \tag{3.5}
$$

with the abbreviated notation $\varphi_n = k_n L_n - B A_n/c$. In Fig. 10 we show one half period of the beats in $T^{\text{tot}}(B) = |t_{11}(B)|^2$ for $[\pi n < B(A_1 - A_2)/(2c) < \pi(n+1)]$, as calculated with Eq. (3.5). The absolute square of the numerator (dashed line, N) and denominator (dotted line D) of Eq. (3.5) display very similar oscillations, both in frequency and amplitude. However, since $T^{\text{tot}} = N/D$, a series of dips are superimposed on the term $\cos^2[B(A_1 - A_2)/(2c)]$ at the points where N and D have their common minima. To classify these dips (i.e., antiresonances) we make use of the fact[28] that the unitarity of Eq. (3.5) can be satisfied by mapping the transport coefficients at the lead junctions (which are assumed to be identical) onto six independent parameters ($r, \epsilon, \phi, \vartheta, \phi_1, \phi_2$),

$$
\tilde{t}_{11} = \tilde{t}'_{11} = \sqrt{\epsilon(1 - r^2)} e^{i[(\phi_1 + \psi)/2 + \vartheta]},
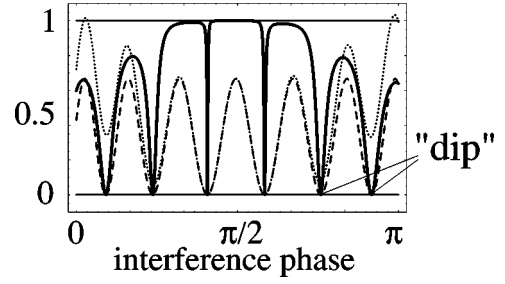$$

FIG. 10. One half period of the beating $\pi n < B(A_1 - A_2)/(2c) < \pi(n+1)$ in the transmission probability $|t_{11}(B/c)|^2$ (solid line), as calculated with our interference model [see Eq. (3.7)]. The numerator (dashed line, N) and denominator (dotted line, D) of $|t_{11}(B/c)|^2$ show very similar oscillations (with a small offset). (N/D) features sharp "dips," at the points where N and D have their common minima. These dips are *window resonances* (also called Breit-Wigner antiresonances) and represent a symmetric limit of the Fano resonance line shape. See the text for details.

$$
\tilde{t}_{12} = \tilde{t}'_{21} = \sqrt{(1 - r^2)(1 - \epsilon)} e^{i[(\phi_2 + \psi)/2 + \vartheta]},
$$

$$
\tilde{r}_{11} = \tilde{r}'_{11} = -[(1 - \epsilon) + \epsilon r] e^{i(\phi_1 + \vartheta)}, \tag{3.6}
$$

$$
\tilde{r}_{12} = \tilde{r}'_{12} = \tilde{r}_{21} = \tilde{r}'_{21} = (1 - r)\sqrt{\epsilon(1 - \epsilon)} e^{i[(\phi_1 + \phi_2)/2 + \vartheta]}
$$

$$
\tilde{r}_{22} = -[\epsilon + (1 - \epsilon)r] e^{i(\phi_2 + \vartheta)}.
$$

Among those, the two parameters ϵ and r are of particular importance in this context. The variable ϵ represents the coupling of the incoming lead state to the edge state $n = 1$ in the interior, and $r \in \mathbb{R}$ is related to the reflection coefficient $\tilde{r}''_{11}$ of an incident channel at the lead mouth, $\tilde{r}''_{11} = r e^{i(\psi + \vartheta)}$. Both quantities $\epsilon, |r|$ are restricted to the interval $[0,1]$. With these terms the absolute square of t_{11} [Eq. (3.5)] can be considerably simplified,

$$
T^{\text{tot}} = |t_{11}|^2 = \frac{(1 - r^2)^2}{|\alpha|^2 |\beta|^2} \frac{\sin^2(\eta/2 + \vartheta_0)}{\sin^2(\eta/2 + \vartheta_0 + \Delta) + \Gamma_0^2}, \tag{3.7}
$$

with $\phi = (\varphi_2 + \phi_2) - (\varphi_1 + \phi_1)$, $\eta = (\varphi_2 + \phi_2) + (\varphi_1 + \phi_1)$, $r' = (1 - \epsilon) e^{-i\phi/2} + \epsilon e^{i\phi/2}$, $\delta = \arg(r')$, $\vartheta_0 = \vartheta + \delta$, $\alpha = 1 + r e^{i(\eta + 2\vartheta)}$, $\beta = 1 + r e^{-2i\delta}$, and $\Delta = \arg(\beta/\alpha)$. The linewidth Γ_0 is given by

$$
\Gamma_0 = \left| \frac{1 - |r'\beta/\alpha|^2}{2r'\beta/\alpha} \right|. \tag{3.8}
$$

In the generic case of $r \neq 0$, resonances occurring in Eq. (3.7) show a typical Fano profile of the form[47]

$$
T^{\text{tot}} \approx |t^{\text{bg}}|^2 \frac{(B/c - B_n/c)^2}{(B/c - B_n/c + \Delta)^2 + \Gamma_0^2}, \tag{3.9}
$$

with t^{bg} being the coefficient for background scattering.[48] The Fano resonances at $B/c = B_n/c - \Delta$ will have an asymmetric line shape unless $\Delta = 0$ (i.e., $r = 0$). This is, however, the case for the billiard systems we consider, since almost no

reflection of incoming lead states takes place at the lead mouths, $\tilde{r}''_{11} \approx 0$, and therefore $r \approx 0$. Under this assumption, Eq. (3.7) simplifies to

$$T^{tot} \approx \frac{\sin^2(\eta/2 + \vartheta_0)}{\sin^2(\eta/2 + \vartheta_0) + \Gamma_0^2}, \qquad (3.10)$$

with linewidth $\Gamma_0 = (1 - |r'|^2)/(2|r'|)$. This equation describes symmetric resonance line shapes, which can be identified as *window resonances* (also called Breit-Wigner dips/antiresonances), of the form

$$T^{tot} \approx \frac{(B/c - B_n/c)^2}{(B/c - B_n/c)^2 + \Gamma_0^2}. \qquad (3.11)$$

The physical picture resulting from this analysis is the following. In the magnetic-field region $B_c^2 \lesssim B \lesssim B_c^1$, where two edge states are present in the interior of the dot and one in each of the leads, the transmission probability shows large-scale oscillations intersected by sharp window resonances. The large-scale envelope function is given by $1/(1 + \Gamma_0^2)$. Its maxima perfectly match with the roughly estimated term $\cos^2[B(A_1 - A_2)/(2c)]$ from above and can therefore be identified with the numbered points in Fig. 7, each of which corresponds to an integer number of longitudinal antinodes in the wave function along the boundary (see Fig. 6). The antiresonances superimposed on these oscillations occur at magnetic fields $B = B_n$ (where $\eta/2 + \vartheta_0 = n\pi, n \in \mathbb{Z}$) and their linewidth is given by Γ_0. As a result, resonances which are situated on maxima of the term $1/(1 + \Gamma_0^2)$ are sharper than at its minima [see the numerical data in Fig. 7 for confirmation]. For an increasing number of edge states populated in the cavity ($B < B_c^2$), our numerical results show that the density of antiresonances is rapidly growing. This behavior finally leads to a resonance overlap for a large number of edge states, which is prerequisite for the onset of Ericson fluctuations (i.e., universal conductance fluctuations).

For completeness, we remark that the above analysis for the B dependence of T^{tot} can analogously be carried out with k_F instead of B as the variable parameter. We can similarly identify threshold values k_c^n for k_F, below which a number of n edge states survive. The numerical results for the transmission probability $T^{tot}(k_F)$ for the case of one or two participating edge states (not shown) can again be described by expressions analogous to Eq. (3.4) or Eq. (3.7).

E. Comparison with experiments

A series of experiments[13,44,49,50] have been performed where Aharonov-Bohm oscillations (ABOs) similar to the ones discussed here have been observed in ballistic transport measurements. The origin of the ABOs in these experiments is, however, twofold. In Refs. 13 and 44, it is the presence of edge states in a quantum dot which gives rise to the observed oscillations. In Refs. 49 and 50 on the contrary, the investigated scattering devices have the form of a ring, to which the scattering wave function is confined. The latter setup thus gives rise to ABOs already at low magnetic fields and has therefore been more readily accessible to a theoretical

description.[51] However, to our knowledge, no quantitative description for magnetotransport through a quantum dot in the regime of only one or two participating edge states has yet become available. We therefore discuss in the following the similarities and differences between the experimental data and our calculations. One important observation is that the magnetic fields where these quasiregular transmission fluctuations appear in the experiment are lower than in the present calculation. For example, in the experiment for circle and stadium shaped quantum dots in a GaAs/AlGaAs-heterostructure,[13] the threshold magnetic-field values would be (in SI units)

$$B_c^n = \frac{2\pi h}{(2n+1)\lambda_F^2 e} \quad \text{with} \quad \lambda_F = \sqrt{\frac{2\pi}{n_s}}. \qquad (3.12)$$

With a given sheet density of $n_s = 3.6 \times 10^{11}$ cm^{-2} in the interior of the dot, the threshold magnetic fields are given by $B_c^2 \approx 3$ T and $B_c^1 \approx 5$ T. However, in the experiment, regular oscillations were already observed below 2 T. At those field values we find highly irregular transmission fluctuations corresponding to a threshold magnetic field B_c^n with $n \gg 1$, indicative of a high density of resonances and Ericson fluctuations. We expect the origin of this discrepancy to lie in the absence of sharp edges in the experiment and, hence, of diffractive edge scattering. In the experimental quantum dot, the edges should be fairly smooth, leading to near-adiabatic transitions to edge states at the entrance to the quantum dot. Therefore fewer edge channels are excited than by diffractive edge scattering, where all energetically accessible channels up to n are populated. Our present results suggest that the observed transmission fluctuations are a direct measure of the sharpness of the edges at the lead mouth. Therefore, investigations of quantum dots with varying sharpness of edges would be desirable. However, since these are difficult to fabricate, we point to a different experimental approach, which is based on the analogy between transport in the edge state regime and field-free transport through a rectangle where only few propagating modes participate.[45] Such structures are accessible for microwave experiments.[6,52] The measured transmission through such a microwave device could provide a stringent test for the multichannel interference model presented above.

IV. SUMMARY AND OUTLOOK

We have presented a technique for calculating ballistic magnetotransport through open quantum dots. The *modular recursive Green's function method* (MRGM) is an extension of the widely used standard recursive Green's-function technique and is based on the decomposition of nonseparable scattering geometries into separable substructures (modules). An unprecedented energy and magnetic-field range can thereby be explored with high accuracy. We applied the MRGM to transport coefficients and scattering wave functions in the two extreme cases of high magnetic fields and short wavelengths. For very small cyclotron radii, we found periodic oscillations in the transmission spectrum and beating phenomena, which are restricted to well-defined intervals

(as a function of B and k_F, likewise). These features could be explained by interferences between edge states, traveling along the boundary of the cavity. For these states scattering only takes place at the lead junctions, whose sharp edges play a crucial role for the dynamics of the system. For a detailed analysis, a multichannel interference model was employed. This model allows us to classify the observed transmission fluctuations in the framework of Fano resonances. For only one edge state present in the circular dot transport is independent of the lead orientation, provided that the lead mouths are identical and separated from each other. Future envisioned applications include the investigation of Andreev billiards,[54] quantum Hamiltonian ratchets,[55] fractal conduc-tance fluctuations,[55,56] and shot noise.[57,58] Furthermore, the MRGM also seems suitable to perform *ab initio* calculations of the integer quantum Hall effect.[59] The challenge is in this case the inclusion of a disorder potential, which is compatible with the separability conditions.

[1] For a review, see, e.g., *The Quantum Hall Effect*, edited by E. Prange and S. M. Girvin (Springer, New York, 1987), and references therein.

[2] M. Büttiker, in *Semiconductors and Semimetals*, edited by M. Reed (Academic Press, San Diego, 1992), Vol. 35, pp. 191–277.

[3] D.R. Hofstadter, Phys. Rev. B **14**, 2239 (1976).

[4] Y. Aharonov and D. Bohm, Phys. Rev. **115**, 485 (1959).

[5] M. C. Gutzwiller, *Chaos in Classical and Quantum Mechanics* (Springer New York, 1991).

[6] H. J. Stöckmann, *Quantum Chaos* (Cambridge University Press, Cambridge, 1999).

[7] E.J. Heller, Phys. Rev. Lett. **53**, 1515 (1984).

[8] X. Yang, H. Ishio, and J. Burgdörfer, Phys. Rev. B **52**, 8219 (1995).

[9] A. MacKinnon and B. Kramer, Z. Phys. B: Condens. Matter **53**, 1 (1983); A. MacKinnon, *ibid.* **59**, 385 (1985); L. Schweitzer, B. Kramer, and A. MacKinnon, *ibid.* **59**, 379 (1985).

[10] S. Rotter, J.-Z. Tang, L. Wirtz, J. Trost, and J. Burgdörfer, Phys. Rev. B **62**, 1950 (2000).

[11] F. Sols, M. Macucci, U. Ravaioli, and K. Hess, J. Appl. Phys. **66**, 3892 (1989).

[12] For a review of the RGM, see, e.g., D. K. Ferry and S. M. Goodnick, *Transport in Nanostructures* (Cambridge University Press, Cambridge, 1997), and references therein.

[13] C.M. Marcus, A.J. Rimberg, R.M. Westervelt, P.F. Hopkins, and A.C. Gossard, Phys. Rev. Lett. **69**, 506 (1992); Surf. Sci. **305**, 480 (1994).

[14] F.P. Simonotti, E. Vergini, and M. Saraceno, Phys. Rev. E **56**, 3859 (1997).

[15] W.E. Bies, L. Kaplan, M.R. Haggerty, and E.J. Heller, Phys. Rev. E **63**, 066214 (2001).

[16] R. Akis, D.K. Ferry, and J.P. Bird, Phys. Rev. Lett. **79**, 123 (1997), I.V. Zozoulenko and T. Lundberg, *ibid.* **81**, 1744 (1998); R. Akis, D.K. Ferry, and J.P. Bird, *ibid.* **81**, 1745 (1998).

[17] I.V. Zozoulenko, F.A. Maaø, and E.H. Hauge, Phys. Rev. B **53**, 7975 (1996); **53**, 7987 (1996); **56**, 4710 (1997).

[18] D. Mamaluy, M. Sabathil, and P. Vogl, J. Appl. Phys. **93**, 4628 (2003).

[19] C.S. Lent, Phys. Rev. B **43**, 4179 (1991).

[20] Z.-L. Ji and K.-F. Berggren, Phys. Rev. B **52**, 1745 (1995).

[21] K. Hornberger and U. Smilansky, Phys. Rev. Lett. **88**, 024101 (2002); Phys. Rep. **367**, 249 (2002).

[22] L. Christenson, H. Linke, P. Omling, P.E. Lindelof, I.V. Zozoulenko, and K.-F. Berggren, Phys. Rev. B **57**, 12 306 (1998).

[23] T. Ueta, J. Phys. Soc. Jpn. **61**, 4314 (1992).

[24] K. Nakamura and H. Ishio, J. Phys. Soc. Jpn. **61**, 3939 (1992).

[25] K. Nakamura, K. Ita, and Y. Takane, J. Phys. A **27**, 5889 (1994).

[26] Y. Wang, J. Wang, and H. Guo, Phys. Rev. B **49**, 1928 (1994).

[27] R.G. Nazmitdinov, K.N. Pichugin, I. Rotter, and P. Šeba, Phys. Rev. B **66**, 085322 (2002).

[28] D.-H. Kim, H.-S. Sim, and K.J. Chang, Phys. Rev. B **64**, 115409 (2001); **67**, 129903(E) (2003); D.-H. Kim and K.J. Chang, *ibid.* **66**, 155402 (2002).

[29] F.M. Peeters, Phys. Rev. Lett. **61**, 589 (1988).

[30] R.L. Schult, H.W. Wyld, and D.G. Ravenhall, Phys. Rev. B **41**, 12 760 (1990).

[31] R.E. Peierls, Z. Phys. **80**, 763 (1933).

[32] H.U. Baranger and A.D. Stone, Phys. Rev. B **40**, 8169 (1989).

[33] T. Ando, Phys. Rev. B **44**, 8017 (1991).

[34] E. N. Economou, *Green's Functions in Quantum Physics* (Springer, Berlin, 1979).

[35] J. Skjånes, E.H. Hauge, and G. Schön, Phys. Rev. B **50**, 8636 (1994).

[36] W. H. Press, S. A. Teukolsky, W. T. Vetterling, and B. P. Flannery, *Numerical Recipes in Fortran 77* (Cambridge University Press, Cambridge, 1986).

[37] N.J. Higham and H.-M. Kim, IMA J. Numer. Anal. **20**, 499 (2000).

[38] H.U. Baranger, D.P. DiVincenzo, R.A. Jalabert, and A.D. Stone, Phys. Rev. B **44**, 10 637 (1991).

[39] H. Ishio and J. Burgdörfer, Phys. Rev. B **51**, 2013 (1995).

[40] J. H. Davies, *The Physics of Low-Dimensional Semiconductors* (Cambridge University Press, Cambridge, 1998).

[41] S. Datta, *Electronic Transport in Mesoscopic Systems* (Cambridge University Press, Cambridge, 1995) and references therein.

[42] L.I. Glazman and M. Jonson, Phys. Rev. B **41**, 10 686 (1990).

[43] U. Sivan, Y. Imry, and C. Hartzstein, Phys. Rev. B **39**, 1242 (1989).

[44] B.J. van Wees *et al.*, Phys. Rev. Lett. **62**, 2523 (1989).

[45] L. Wirtz, C. Stampfer, S. Rotter, and J. Burgdörfer, Phys. Rev. E **67**, 016206 (2003).

[46] L. Wirtz, J.-Z. Tang, and J. Burgdörfer, Phys. Rev. B **59**, 2956 (1999).

[47] U. Fano, Phys. Rev. **124**, 1866 (1961).

[48] J.U. Nöckel and A.D. Stone, Phys. Rev. B **50**, 17 415 (1994).

[49] R.A. Webb, S. Washburn, C.P. Umbach, and R.B. Laibowitz, Phys. Rev. Lett. **54**, 2696 (1985).

[50] S. Pedersen, A.E. Hansen, A. Kristensen, C.B. Sørensen, and P.E. Lindelof, Phys. Rev. B **61**, 5457 (2000).

[51] K.N. Pichugin and A.F. Sadreev, Phys. Rev. B **56**, 9662 (1997).

[52] T. Blomquist, H. Schanze, I.V. Zozoulenko, and H.-J. Stöckmann, Phys. Rev. E **66**, 026217 (2002).

[53] J. Cserti, A. Kormányos, Z. Kaufmann, J. Koltai, and C.J. Lambert, Phys. Rev. Lett. **89**, 057001 (2002).

[54] H. Schanz, M.-F. Otto, R. Ketzmerick, and T. Dittrich, Phys. Rev. Lett. **87**, 070601 (2001).

[55] R. Ketzmerick, Phys. Rev. B **54**, 10 841 (1996).

[56] A. Bäcker, A. Manze, B. Huckestein, and R. Ketzmerick, Phys. Rev. E **66**, 016211 (2002).

[57] Y.M. Blanter and M. Büttiker, Phys. Rep. **336**, 1 (2000).

[58] S. Oberholzer, E.V. Sukhorukov, and C. Schönenberger, Nature (London) **415**, 765 (2002).

[59] T. Koschny, H. Potempa, and L. Schweitzer, Phys. Rev. Lett. **86**, 3863 (2001).